Received: 2 January 2024 | Revised: 21 April 2024 | Accepted: 28 April 2024

DOI: 10.1002/sia.7321

RESEARCH ARTICLE

SURFACE and INTERFACE ANALYSIS WILEY

Correlating corrosion modes with the microstructure of the 2XXX series alloys: A comparative approach

Rafael Emil Klumpp[1,2] | Sajjad Akbarzadeh[2,3] | João Victor de Sousa Araujo[1] | Maurice François Gonon[2] | Fabienne Delaunois[3] | Isolda Costa[1] | Marie-Georges Olivier[2]

[1]Instituto de Pesquisas Energéticas e Nucleares, Av. Prof. Lineu Prestes, 2242, São Paulo, CEP 05508-000, Brazil

[2]Materials Science Department, Faculty of Engineering, University of Mons, 20, Place du Parc, Mons, 7000, Belgium

[3]Metallurgy Department, Faculty of Engineering, University of Mons, 20, Place du Parc, Mons, 7000, Belgium

Correspondence
Rafael Emil Klumpp, Materials Science Department, Faculty of Engineering, University of Mons, 20, Place du Parc, 7000 Mons, Belgium.
Email: rafaelemil.klumpp@umons.ac.be

Funding information
CNPq, Grant/Award Numbers: 406871/2021-3, 200257/2022-6; SPW-Economie Emploi Recherche – Wallonie in the framework of the program OptiSurFam – Win2Wal, Grant/Award Number: 2310020; Fundação de Amparo à Pesquisa do Estado de São Paulo, Grant/Award Number: 2019/18388-1; Fédération Wallonie-Bruxelles

In this study, the localized corrosion susceptibility of AA2050-T84, AA2198-T851, and AA2024-T3 alloys was compared by immersion in three test solutions, specifically sodium chloride solution (3.5% NaCl), EXCO solution, according to ASTM G34-18, and a solution for intergranular corrosion (IGC) test recommended by ASTM G110-15 and via scanning vibrating electrode technique (SVET). The results showed higher susceptibility of AA2050-T84 alloy to all types of corrosion tested compared to the other studied 2XXX series alloys. Corrosion penetration was deeper in the AA2050-T84 due to its microstructural characteristics as a difference in the micrometric Cu-Rich intermetallic particle distribution on the surface and related to the distribution of the T1 (Al_2CuLi) phase.

KEYWORDS
aluminum alloys, immersion tests, localized corrosion, microstructure, SVET

1 | INTRODUCTION

Reducing fossil fuel consumption, consequently, greenhouse gas emission, is a critical target in the transport and aircraft sectors. In this sense, weight reduction is an efficient way to reach these goals.[1] Research has been carried out to develop new Al alloys with lower weight compared to commercial alloys. The addition of Li replacing some of the alloying elements is one of the possibilities.

Al alloys have a crucial role in the aerospace sector.[1,2] Al alloys' strength and lightweight characteristics are the reasons for being used as materials for aircraft fabrication for more than 80 years.[1,3]

The Al-Cu-Li alloys have been developed over the last decades due to their decreased weight compared to the commercial Al alloys from the 2xxx series.[1,2] The efforts aim to reduce fossil fuel consumption and, consequently, CO_2 emissions. In this context, the new generation of Al–Cu-Li alloys has been developed with the purpose of replacing conventional alloys from the high-strength 2XXX and 7XXX series.[2] The AA2050-T84 is a new Al-Cu-Li alloy generation with a lower density than the conventional alloys from the 2XXX series. The addition of lithium (density of 0.54 $g.cm^{-3}$) as an alloying element is of interest due to its high solubility in aluminum.[2,4] Each 1% of Li added to the aluminum alloy leads to a 3% reduction in the alloy density and an increase of 6% in the alloy modulus of elasticity.[1,4] However, intermetallic (IM) precipitates result from the addition of alloying elements, giving rise to complex microstructures and increased heterogeneity, favoring corrosion. Due to the high activity of lithium, the new generation of Al-Cu-Li alloys is highly susceptible to localized

corrosion[5–9] that affects the aesthetics of parts and, more crucially, the integrity of structures that are subjected to fatigue and/or static stresses and then can result in catastrophic failures,[10,11] especially when these alloys are used in wing and/or fuselage structures.

The localized corrosion susceptibility of the Al-Cu-Li alloys is mainly associated with the hexagonal T1 phase (Al-Cu-Li) located preferentially in regions with high density of dislocations.[9,12–20] According to the literature, the T1 phase (Al-Cu-Li) is initially anodic relative to the matrix,[8,13,21] because of its high reactivity, Li is preferentially dissolved resulting in copper enrichment, leading to reversal polarity, and, ultimately, to dissolution of the Al matrix.[8,13,22,23] The literature indicates development of severe localized corrosion in Al-Cu-Li alloys when exposed a corrosive solutions.[17,24,25] Machado et al[24] displayed the development of severe localized corrosion on AA2198-T851 even in low concentration sodium chloride solution (0.001 M). Milagre et al showed severe types of corrosion, pitting, trenching, and intergranular attack, on the AA2098-T351 after exposition in 0.005 Mxl^{-1}NaCl. Da Silva et al[25] showed the influence of the near-surface deformed layer present in this alloy (AA2098-T351) that decreased the local electrochemical activity on the surface when compared with the polished one, both exposed in NaCl 0.005 M solution. On the other hand, Alexopoulos et al[26] indicate that the tensile properties for AA2024 T3 are more affected by exposition in Exco solution than AA 2198-T3 alloy indicating a superior corrosion degradation resistance for the Al-Cu-Li alloy.

As mentioned earlier, the AA2050 alloy was developed to replace the AA2XXX alloys, however, not many studies are comparing the corrosion behavior of AA2050, especially with the one of the AA2024 and AA2198 alloys. The AA2024 is an Al–Cu-Mg alloy widely employed in the aircraft manufacturing sector. This alloy presents a complex microstructure with the presence of coarse Cu-rich intermetallic particles (cathodic to the matrix) and S-phase (Al-Cu-Mg) that selective Mg corrosion converts from anodic to cathodic to the matrix.[27–31] The AA2198 is one alloy of Al-Cu-Li third generation as AA2050, and presents a similar density (2.70% for AA2050 and 2.69% for AA2198) and Li content (1%), although it has a smaller amount of Cu (3.5% for AA2050 and 3.3% for AA2198).[32] As a result, the AA2198 has a complex microstructure with micrometric Cu-rich precipitates and a nanometric T1 (Al_2CuLi) phase. This alloy is associated with the highest susceptibility to severe localized corrosion.[7,18,33,34] This justifies its selection for comparison.

In this work, the distinct localized corrosion behavior of the new generation Al-Cu-Li AA2050-T84 was compared with that of the commercial AA2198-T851 and AA2024-T3 alloys by exposure to various test solutions followed by analysis of the exposed surfaces. It explored how precipitates, both at micro and nanoscales, affect the corrosion resistance of aluminum alloys. In an aqueous corrosive medium, a relationship between composition, particle distribution, and corrosion resistance is determined.

2 | EXPERIMENTAL

2.1 | Materials

Plates of the AA2050 (Al-3.5Cu-1Li-0.3 Mg-0.04Fe-0.08Si-0.5Ag-0.11Zr[wt.%]) alloy with 6 mm thick was employed in this investigation. The metallurgical conditions of the AA2050 rolled plates were T84, which corresponds to a heat treatment at 520°C for 60 minutes followed by water quenching at 25°C. After quenching, the alloy was submitted to cold work (a plastic strain of 4%) and artificial aging at (155 ± 5) °C for 18 hours.[35,36]

For comparison, the AA2198-T851 (Al- 3.31-Cu 0.96 Li - 0.31 Mg - 0.03 Si - 0.04 Fe - 0.25 Ag - 0.4 Zr - 0.01 Zn [wt. %]) and AA2024-T3 (Al-4.5 Cu-1.41 Mg-0.61 Mn-0.12 Fe-0.03 Zn [wt.%]) alloys were tested. The Al-Cu-Li samples (AA2050 and AA2198) were supplied by Constellium.

All the samples were sequentially polished to a 1 μm surface finishing using SiC papers and diamond pastes before any test. For the macrographs, in order to reveal the grain boundaries, the sample was exposed for 15 s to Weck's reagent (1 g NaOH + 4 g $KMnO_4$ + 100 ml deionized water) for a metallography attack.

2.2 | Immersion tests

Immersion tests were carried out in the following solutions and conditions: (i) naturally aerated 3.5% NaCl solution at room temperature for 72 h; (ii) EXCO solution (4 mol L^{-1} NaCl + 0.5 mol L^{-1} KNO_3 + 0.1 mol L^{-1} HNO_3) for exfoliation corrosion test performed according to ASTM G34–2018. The samples were immersed in this solution for 6 h and 24 h; (iii) IGC test solution (1 mol L^{-1} NaCl + 10 ml of H_2O_2 [30%]/L) for corrosion immersion tests according to ASTM G110–2015 for 6 h. In order to evaluate the corrosion evolution in sodium chloride solution ofAA2050, a naturally aerated 0.1 mol L^{-1} NaCl solution at room temperature for 24 h and 48 h exposition time was used.

Weight loss of the specimens was carried out according to ASTM G 34 before and after exposure to the Exco solution.

2.3 | Macro and microstructure examination

For the determination of the particles per surface area, the software ImageJ was used to count the micrometric intermetallic (IM) particles from the SEM Images of alloy surfaces.

Macro and microstructural characterizations of the alloys were carried out by optical microscopy (OM) using a KH 8700 Hirox Digital Microscope, and scanning electron microscopy (SEM-FEG) using a Model SU8020 microscope, equipped with an energy-dispersive X-ray spectroscopy (EDX) detector.

X-ray diffraction analyses (XRD) were performed using a Panalytical Empyrean diffractometer, operating in Bragg–Brentano geometry

with a CuKα1 radiation (λ = 0.1540598 nm). Patterns were recorded from 10° to 100° with a step size of 0.026° and a dwell time of 1 s per step.

2.4 | Localized electrochemical evaluation

The localized corrosion characteristics were further assessed via scanning vibrating electrode technique (SVET) in a 15mM NaCl electrolyte, employing an applicable electronics instrument. The panels were prepared for the cut-edge configuration by being embedded in epoxy resin (EpoFix), and then mechanically polished with 800, 1,200, 2,400, and 4,800 grit size sandpapers. By using 3 M™ Scotchrap™ 50 tape, the exposed surface area of the samples was set at around 3 mm^2. To increase the tip capacitance, the platinum/iridium SVET probe with 20 μm diameter was platinized in a solution comprising 10% (wt/wt) platinum chloride and 1% (wt/wt) lead (II) acetate. Thereafter, following the instrument instruction manual, the SVET calibration was carried out using a 15mM NaCl (604 Ω cm resistivity) solution. The operational parameters were 40 μm, 60 Hz, and 200 μm corresponding to vibration amplitude, vibration frequency, and vibrating electrode distance from the sample, respectively. To assure the precision of the results, at least two SVET measurements with 31 × 31 grid points were conducted.

3 | RESULTS

Figure 1A shows the AA2050-T84 surface, which is composed of equiaxed grains with a mean grain size of ∼ 28 μm, according to ASTM E 122. Figure 1B displays the surface of AA2050 with the presence of coarse IM particles. In order to identify the composition of the coarse IM particles, EDX analysis was carried out in the particles as indicated in Figure 1C, and the results are presented in Table 1, which shows these micrometric particles are mainly composed of Al, Cu, Fe, and Mn, and have a mean Cu/Fe ratio of 3.2. The EDX map of a micrometric particle in the AA2050-T84 is shown in Figure 2 showing that these are Cu, Fe, and Mn enriched.

Figure 3A displays the XRD patterns for the Al alloys' surface. For the three alloys the identified phases correspond to a face-centered cubic (FCC) and the Al peaks were indexed to the hkl lattice plane (111), (200), (220), and (311), this last also could be attributed to θ-Al_2Cu. For the Al-Cu-Li alloys (AA2198 and AA2050), two additional peaks are detected for 2 theta angles at ∼ 42° (with a medium intensity) and ∼ 21° (with a weak intensity). Both peaks match with Al_2CuLi, but also with θ-Al_2Cu for the peak at ∼ 21°. A similar XRD pattern was found by Jagadeesh *et al*[37] for the AA2050 alloy obtained by different forging routes. This is due to the main hardening phase in this alloy, that is, the nanometric T1 (Al_2CuLi). This phase results from metastable precursors, such as θ (Al_2Cu), T_2 (Al_5Li_3Cu), T_B (Al_7Cu_4Li), S (Al_2CuMg), and δ (Al_3Li).[38]

Figure 4 displays the cross-section view of the alloy's after 6 h of exposure to the IGC solution (ASTM G110). Figure 4A shows severe localized corrosion composed of cavities and trenches on all exposed surfaces of the AA2050-T84. The attack propagated along the grain boundaries and penetrated the alloy reaching depths of nearly 107 μm. The AA2050 alloy presented a selective corrosion attack at grains, that spread by intergranular but also transgranular corrosion. The literature indicates that susceptibility to IGC is due to the nanometric T1 phase located mainly at dislocations.[5,9,33,39] In the same sense, the cross-section view of the exposed surface of the AA2198-T851, Figure 4B displayed intergranular and transgranular attacks, although attack spreads laterally affecting lower areas (around 166 μm) than for the AA2050 (around 387 μm) and the penetration was less deep (around 79 μm) compared to the AA2050 (107 μm).

TABLE 1 Micrometric particle composition estimated by EDX measurements.

Weight %	C-K	O-K	Al-K	Mn-K	Fe-K	Cu-K
pt1	4.0		51.4	5.1	9.1	30.4
pt2	3.6		54.5	2.7	8.9	30.3
pt3	3.6	1.7	56.8	2.5	9.7	25.8
pt4	3.4		62.0	14.3	4.5	15.8
pt5	3.9	2.9	74.5	1.8	3.8	13.1

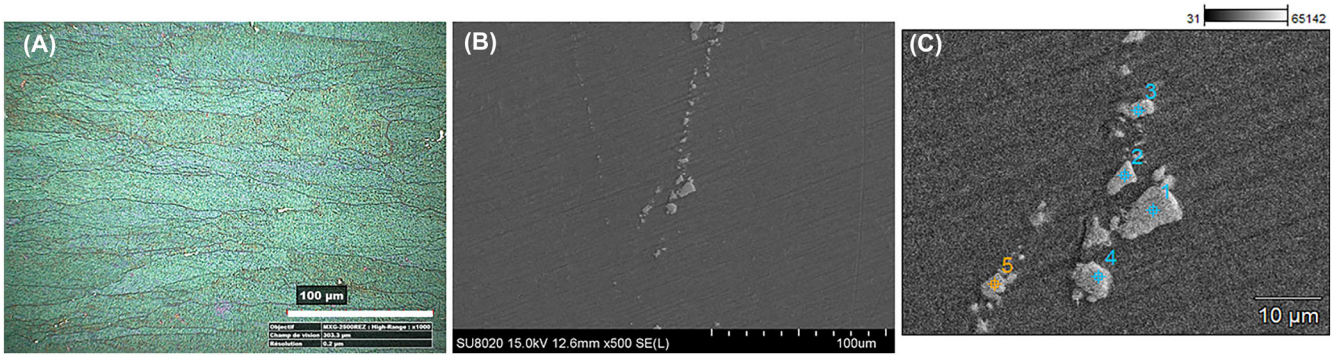

FIGURE 1 Micro and macrographs of the AA2050-T84 alloy surface.

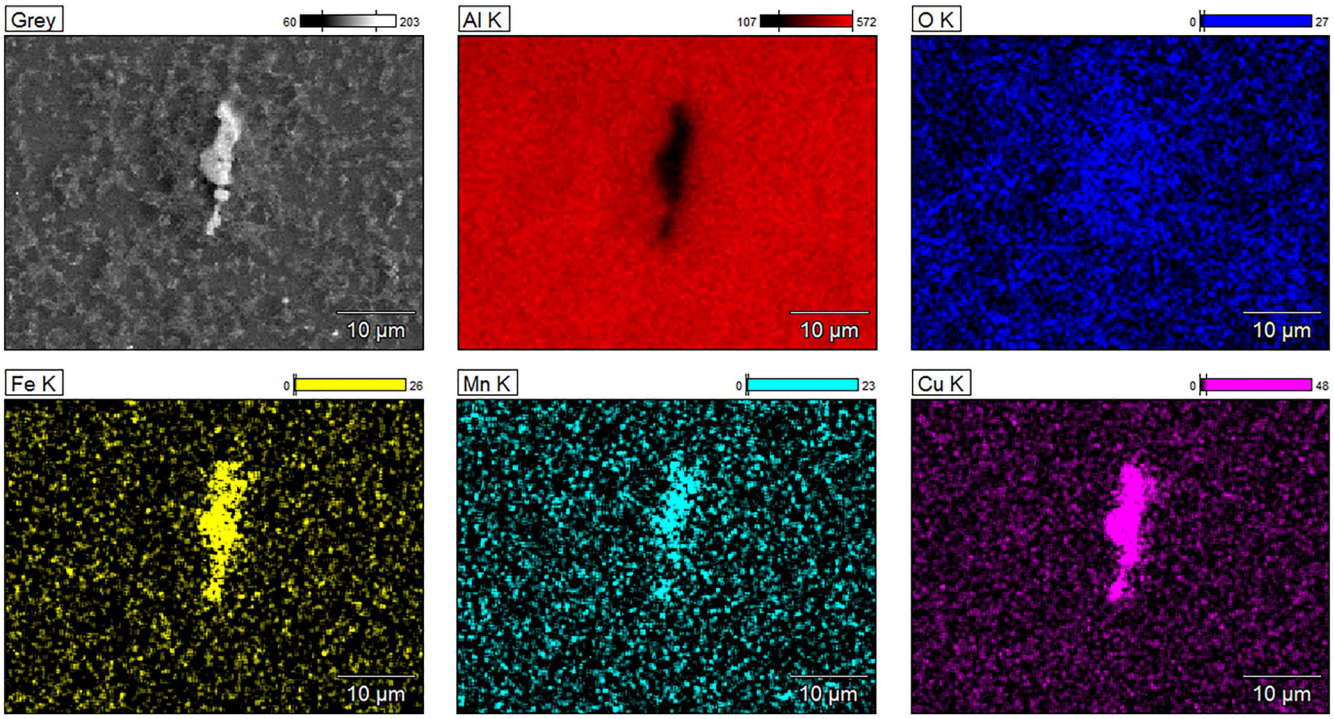

FIGURE 2 Elemental EDX map of micrometric particle in the AA2050-T84 alloy surface.

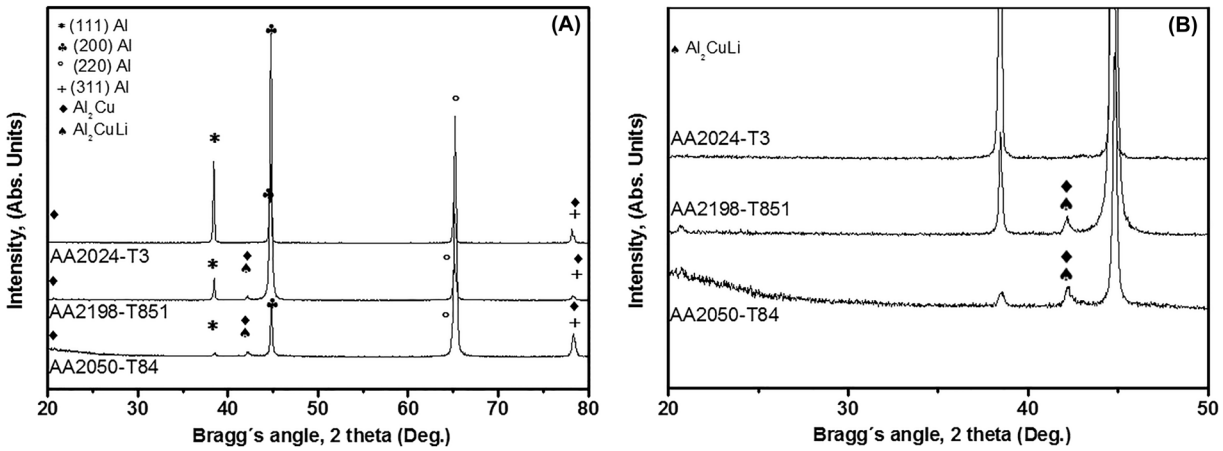

FIGURE 3 XRD pattern of alloy surfaces (a) and (b) Al2LiCu XRD peak comparison plot.

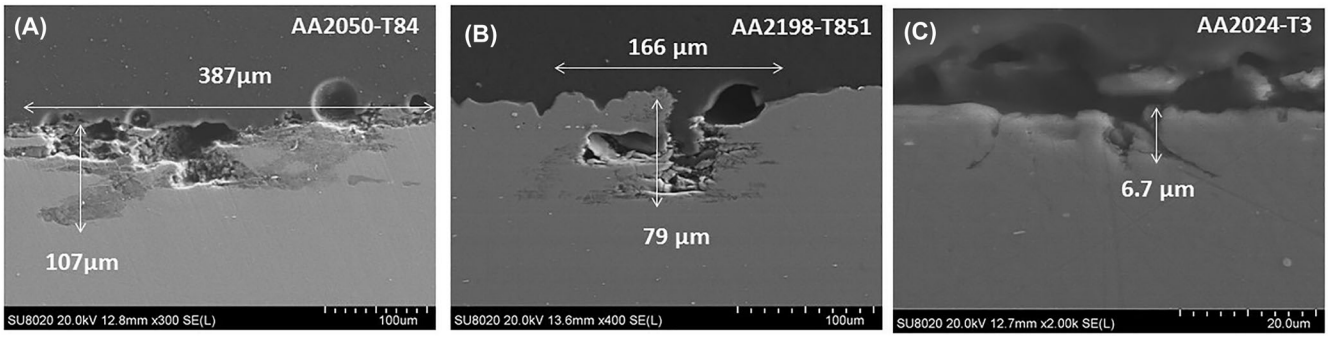

FIGURE 4 SEM micrograph of the cross-section of the exposed surface after immersion in the intergranular corrosion test (IGC) solution (ASTM G110); AA2050-T84 (A), AA2198-T851 (B), and AA2024-T3 (C).

The AA2024-T3 is also susceptible to IGC attack due to the S-phase (Al_2CuMg) mainly at the grain boundaries.[6–8,22] The cross-section view of the surface of the AA2024-T3 exposed to the IGC solution, Figure 4C, displays the smaller areas with less corrosion attack and lower penetration (around 6.7 μm). This difference indicates the higher tendency of severe localized corrosion in the Al-Cu-Li alloys compared to the Al-Cu-Mg ones (AA2024). The results of this study are supported by the literature that showed that the presence of Cu and Fe-enriched IM particles, cathodic to the matrix, favor nucleation of localized corrosion.[8,12,40–42]

The exposed surface of the tested alloys after 6 h of immersion in the exfoliation corrosion test (EXCO) solution (ASTM G34) is presented in Figure 5. The AA2050-T84 (Figure 5A) presents a severe attack indicating its high susceptibility to exfoliation.

The depth of penetration of the corrosion attack was approximately 179 μm. The penetration occurred through the grain boundaries. The cross-section view of the AA2198-T851 (Figure 5B) displayed severe localized intergranular and transgranular attacks. However, the attack was less aggressive than for the AA2050 and penetration was less deep (around 22.4 μm). As in the IGC test, AA2024-T3 (Figure 5C) displayed the lowest areas affected by corrosion among the tested ones, with a depth of corrosion penetration of around 5 μm. These results are in accordance with the literature. Araujo et al[7] who studied the resistance to exfoliation and intergranular corrosion (IGC) of the AA2198 alloy and compared it with AA2024 indicated that AA2024-T3 alloy is more resistant to exfoliation corrosion.

The results of weight-loss measurements after 24 h of exposure to EXCO solution are shown in Figure 6. The weight-loss corresponding to the AA2050-T84, AA2198-T851, and AA2024-T3 were 74.8 g/m^2, 39.7 g/m^2, and 15.3 g/m^2, respectively. This result is in accordance with the depth of corrosion penetration observed in Figures 4 and 5 and is easily observed when comparing the cross-sectional macrographs of the three alloys tested. The AA2050-T84 presents higher susceptibility to exfoliation compared to the other 2XXX alloys, Figure 5. Exfoliation penetration in the AA2050-T84 was several times deeper than for the AA2024-T3. A comparison of the IGC susceptibility of the alloys also showed that the AA2050-T84 presented a higher tendency to this type of attack, Figure 4. These results are in accordance with the literature. Araujo et al[7] presented the susceptibility of IGC of Al-Cu-Li alloys and indicated that AA2024-T3 alloy is more resistant to exfoliation corrosion. The low resistance to exfoliation is mainly due to the nanometric T1 phase that is preferentially located at the dislocations inside the more deformed grains favoring IGC, exfoliation corrosion, and severe localized corrosion.[5,9,33,39]

The exposed surface of the alloys after 72 h of immersion in NaCl 3.5% solution is presented in Figure 7. AA2050-T84 sample, Figure 7A, presented severe localized corrosion that propagated under the exposed surface, resulting in detachment of material from the surface. The corrosion process propagated through the grains resulting predominantly in transgranular attack (red arrow) but also intergranular corrosion (yellow arrow). At high magnification, the transgranular attack is easily observed, Figure 7D, leading a several alloy material consumption. A severe localized attack is also observed on the surface of the AA2198-T851 after immersion in NaCl 3.5% solution, Figure 7B,E. In the same way, intergranular and transgranular attacks were observed spreading along the deformation direction. The AA2024-T3 after immersion in NaCl 3.5% solution (Figure 7A,F) presented corrosion penetration around (16 μm), lower than for the AA2050 (44 μm), and AA2198 (24 μm). The results are in accordance

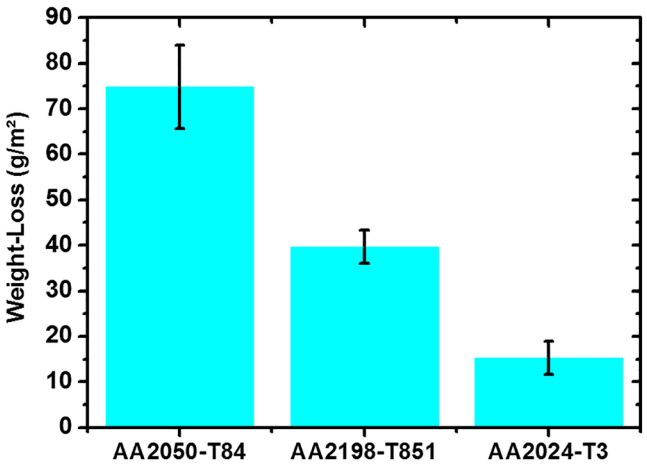

FIGURE 6 Weight-loss for immersion test in the exfoliation corrosion test (EXCO) solution (ASTM G34).

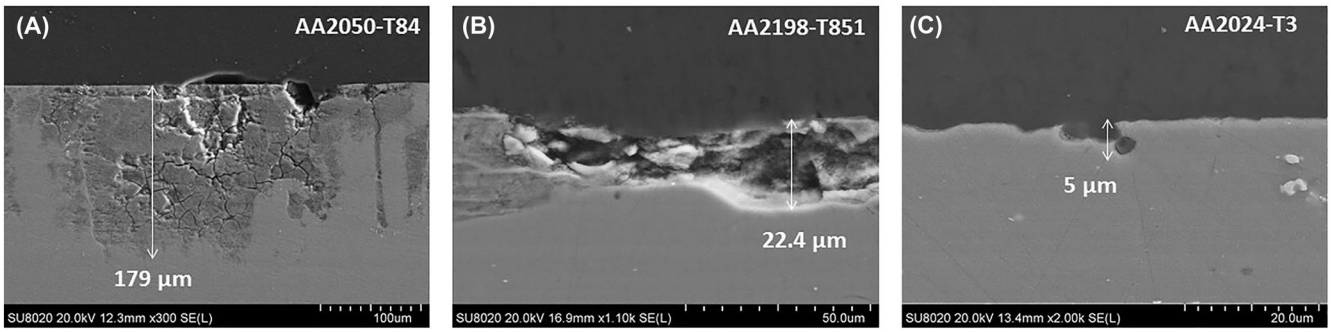

FIGURE 5 SEM micrograph of the cross-section of the exposed surface after immersion in the exfoliation corrosion test (EXCO) solution (ASTM G34); AA2050-T84 (A), AA2198-T851 (B), and AA2024-T3 (C).

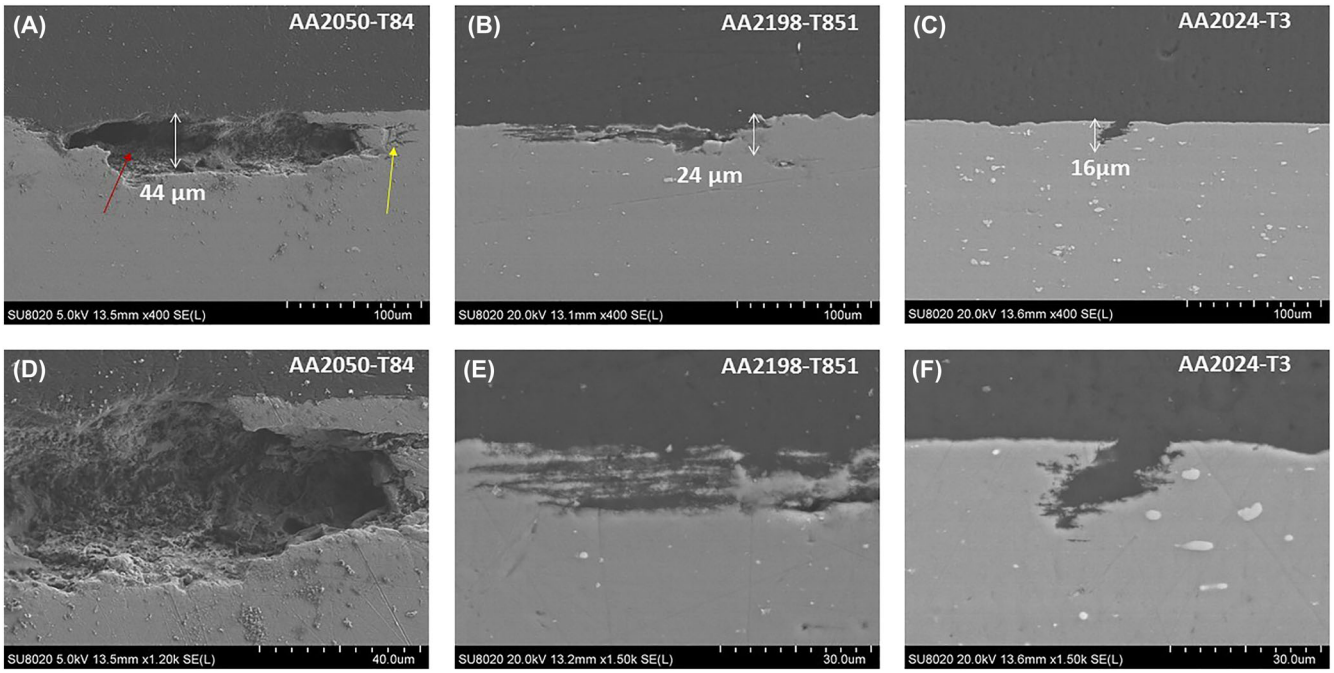

FIGURE 7 SEM micrograph of the cross-section of the surface of the alloy after immersion in naturally aerated 3.5 (wt.%) NaCl solution; AA2050-T84 (A), AA2198-T851 (B), AA2024-T3 (C), AA2050-T84 (D), AA2198-T851 (E), and AA2024-T3 (F).

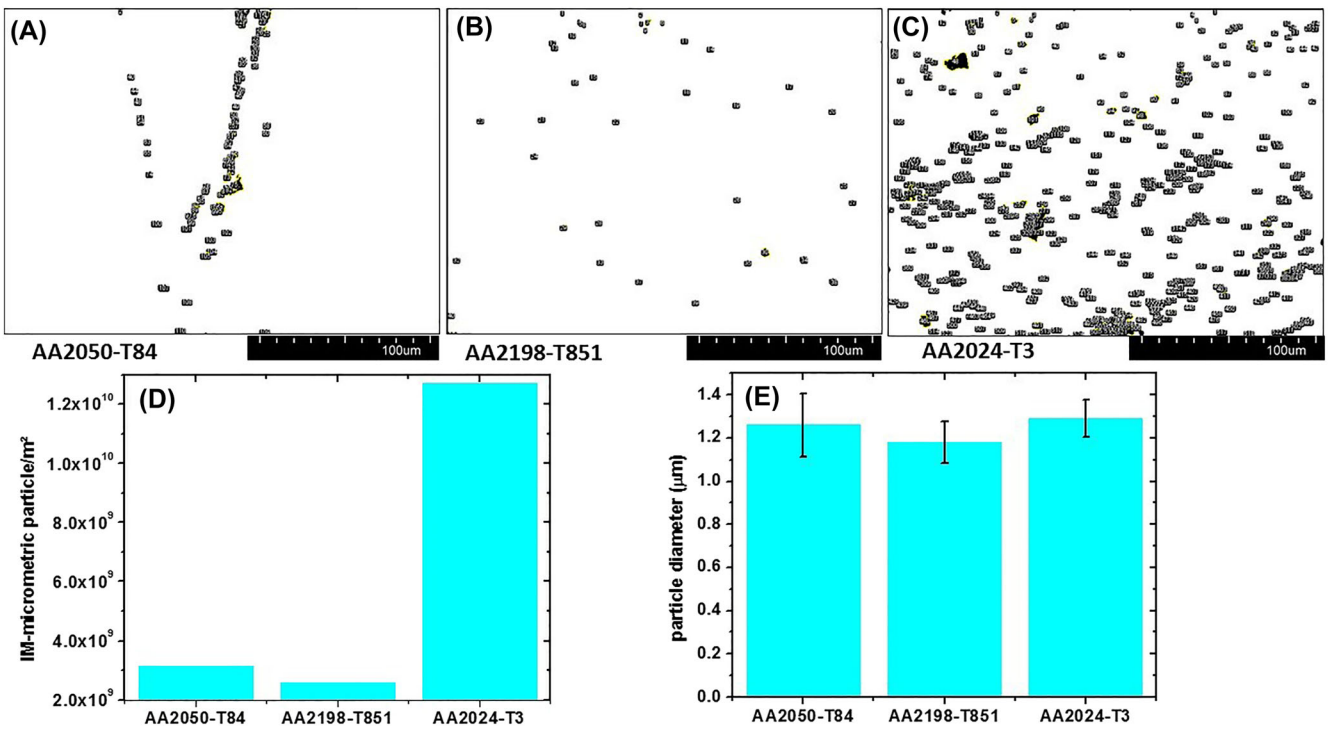

FIGURE 8 Threshold treated SEM images of studied alloys; AA2050-T84 (A), AA2198-T851 (B), AA2024-T3 (C), comparison of number of micrometric particles per area (D), and particle diameter comparison (E).

with the other used tests suggesting a special role of the T1 phase in the severe corrosion development tendency.

To better understand the differences presented in the immersion corrosion tests, the distribution of coarse intermetallic (IM) particles in the alloys is presented in Figure 8. The threshold-treated image of AA2050-T84, AA2198-T851, and AA2024 surface alloys are displayed in Figure 8A–C, respectively, in order to compare the characteristics of the particles at the surface. It is worth mentioning that the

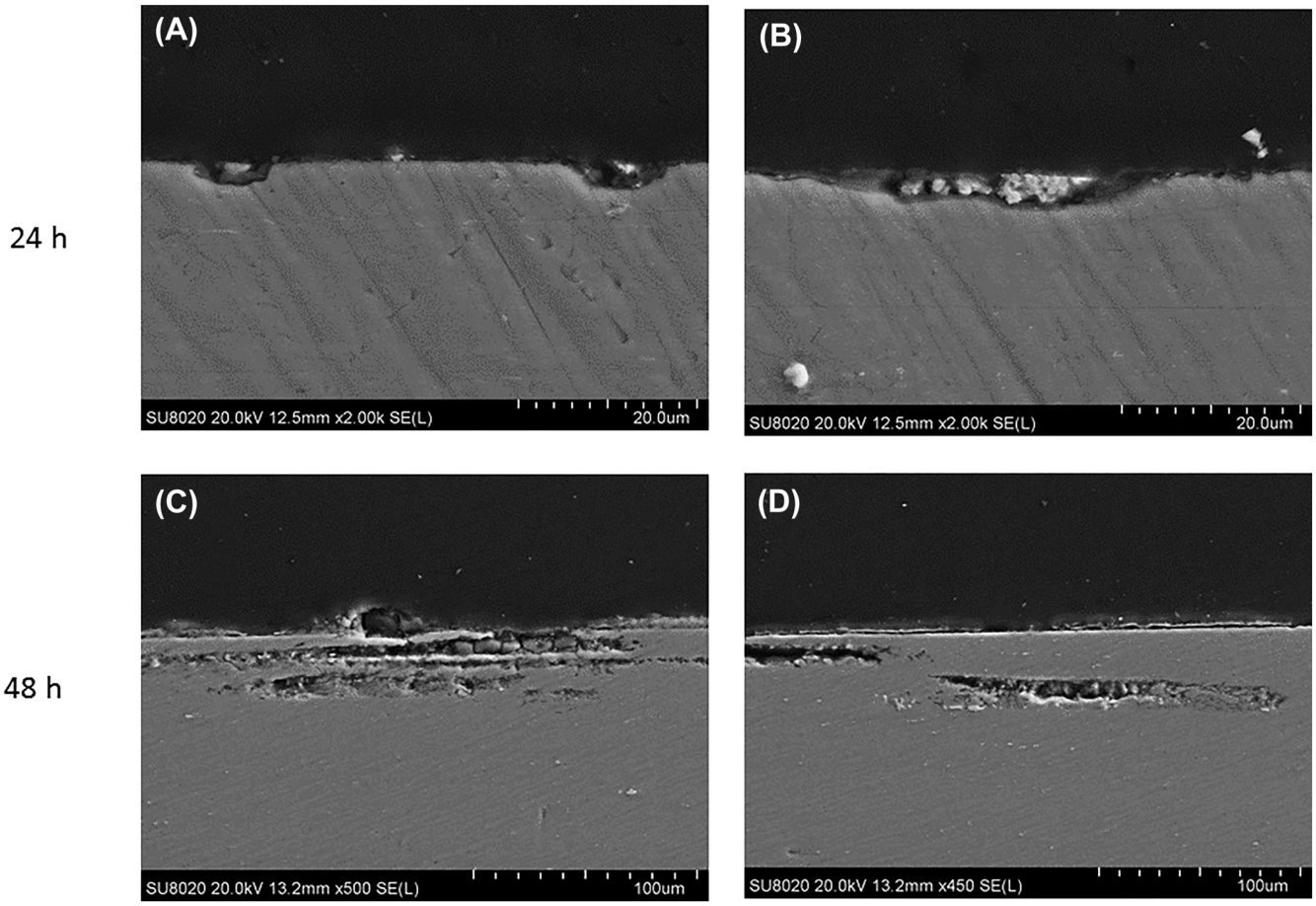

FIGURE 9 SEM images of the cross-section of AA2050-T84 surface after immersion (24 h and 48 h) in naturally aerated 0.1 Mol L^{-1} NaCl solution.

alloys show differences in the distribution and quantity of micrometric intermetallic at the surface. The AA2024-T3 (Figure 8C), displayed the highest number of particles per area ($1.27x10^{10}$ IM-micrometric particles/m^2). The AA2050 presented $3.15x10^9$ IM-micrometric particles/m^2 and the AA2198-T851, 2.57 $15x10^9$ IM-micrometric particles/m^2. The comparison is presented in Figure 8D. The distribution of the particles in the three tested alloys also differs. The AA2050 showed agglomeration of the particles, while the particles in the AA2198-T851 were distributed along the surface. The IM-particle diameters were compared, and the alloys presented similar mean diameters, Figure 8E.

In order to evaluate the evolution of the severe localized corrosion in the AA2050-T84, a sample was exposed to 0.1 mol L^{-1} NaCl solution for 24 h and 48 h. The exposed surface is presented in Figure 9. Localized corrosion starts with trenching surrounding the IM- -micrometric particles (Figure 9A,B), which are Cu and Fe-rich, Figure 2. In Figure 9C, the surface exposed for 48 h to 0.1 mol L^{-1} NaCl solution indicates that the corrosion propagated under the exposed surface laterally and resulted in material detachment from the surface. The propagation occurs through the grain boundaries and results in intergranular attack and transgranular corrosion.

The SVET maps along with the optical images of different grades of aluminum alloys after 16 hours of immersion in 15mM NaCl electrolyte are presented in Figure 10. The SVET results were obtained using the cut-edge design, resulting in approximately a 3 mm^2 exposed area for the coated samples. The susceptibility of all alloys to local corrosion is evident by the presence of anodic spots (red regions). For AA2024, galvanic corrosion resulted from the existence of Cu-rich IM particles in the aluminum body. Since the passive layer on these particles has poor resistive qualities, AA2024 is vulnerable to localized corrosion, which reveals the substrate to the aggressive electrolyte. The anodic region was enlarged during the exposure as the corrosion phenomenon progressed. In the case of Al-Cu-Li alloys, the presence of T1 and T2 precipitates led to their preferential dissolution as they acted as anodic zones. The potential difference between these precipitates and the aluminum matrix resulted in preferential corrosion. For AA2198, localized corrosion was recorded with a significant enhancement in the current density compared to AA2024. Meanwhile, AA2050 exhibited more anodic spots, indicating more severe localized corrosion. The differing vulnerability to localized corrosion observed between AA2050 and AA2198 (both Al-Cu-Li alloys) might be attributed to differences in the dispersion of

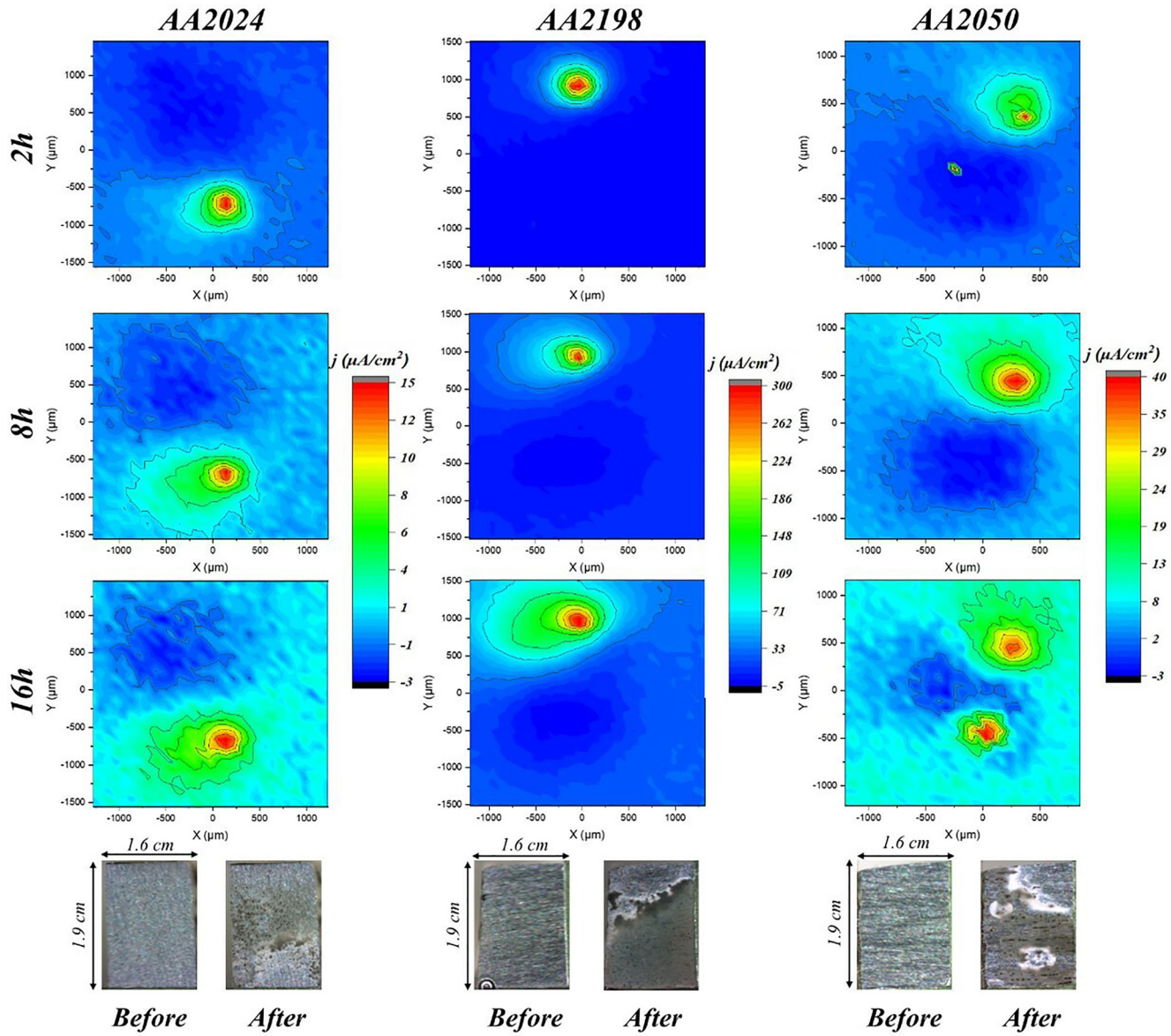

FIGURE 10 SVET maps of AA2024, AA2198, and AA2050 alloys after 16 h immersion in 15mM NaCl electrolyte.

intermetallic particles within these alloys. Notably, AA2050 demonstrates a greater density of particles per unit area than AA2198, making it more vulnerable to localized corrosion. The optical images obtained at the end of the immersion test corroborated the SVET maps and poor corrosion resistance of Al-Cu-Li alloys to the localized corrosion.

4 | DISCUSSION

The results presented in this work showed higher susceptibility of the Al-Cu-Li alloys to all types of corrosion tested compared to the AA2024-T3. In this sense, the results pointed out the highest susceptibility of the AA2050-T84 to severe localized corrosion.

The susceptibility of the Al-Cu-Li alloys to the development of severe localized corrosion is well known.[5,12,18,20,23,40,43–45] This observation was also confirmed in this study by immersion in various solution tests (IGC, EXCO, and NaCl solution) and SVET maps, Figures 4–7, 9, and 10. As indicated in Figure 1, the AA2050 surface has Cu-rich coarse IM particles distributed in the alloy. The copper-rich particles have a special role in corrosion nucleation and propagation. The cathodic behavior of these particles relative to the aluminum matrix is well established[8,22,39,44] θ (Al_2Cu) and Fe-Cu-rich coarse IM particles can sustain a large cathodic current and are associated with pitting.[8] These particles are responsible for a selective dissolution associated with pitting formation.[8,22]

Figure 9A,B shows anodic dissolution surrounding coarse IM particles. The severe localized corrosion starts at sites of high

TABLE 2 Immersion tests summary.

Alloy	ASTM G110	Penetration (μm)	ASTM G34	Penetration (μm)	Weight-loss (g/m^2) after 24 h	NaCl 3.5%	Penetration (μm)
AA2024	Intergranular attack.	6.7	exfoliation in lowest areas	5.0	15.3	Severe localized corrosion - intergranular and transgranular attack	16.0
AA2198	Severe localized corrosion that spreads by intergranular and transgranular attack.	79.0	Severe exfoliation	22.4	39.7	Severe localized corrosion that spreads by intergranular and transgranular attack.	24.0
AA2050	Severe localized corrosion that spreads by intergranular and transgranular attack.	107.0	Severe exfoliation	179.0	74.8	Severe localized corrosion that spreads by intergranular and transgranular attack.	44.0

concentration of IM particles after the dissolution of the thin anodic superficial film (naturally air-formed Al_2O_3) in contact with the corrosive environment. Due to Cl^- in the corrosive environment, damage to the oxide film occurs leading to nucleation of pitting. The IM coarse particles, initially cathodic sites, represent a lower area compared to the matrix (anodic sites). The galvanic effect initiates localized corrosion due to potential differences. Buchheit et al[22] showed a Cu-depleted zone around S-phase IM particles, formed during heat treatment. The IM particles are not redissolved during solidification. This increases alloy heterogeneity and, consequently, the galvanic effect. The anodic dissolution observed in Figure 9C,D and the SVET maps correspond to the Cu-depleted zone. As it is well known, the corrosion propagation of Al alloys is autocatalytic. In the case of Al-Cu-Li alloys, several authors have reported the presence of nanometric T1 phase (Al_2CuLi) at their grain boundaries.[5,8,12,34,40] The dissolution of this phase is accelerated due to the increasingly aggressive environment inside the cavities and initiated by micro galvanic effects. This leads to IGC and sub-grain boundary attack, as is easily observed in Figures 4 to 5 where IGC and exfoliation corrosion are highlighted.

Similarly, to the S-phase (Al_2CuMg), the T1 phase (Al_2CuLi) corrodes preferentially by initial leaching of Li (selective Li dissolution). This selective dissolution leads to a Cu-rich remnant that is eventually released into the electrolyte. This Cu is in the free corrosion potential and ionizes.[6,8,22] As indicated in the pieces of literature the Cu ions are redeposited, acting as micro-cathodes.[6,8,22] This situation corresponds to very small cathodic areas embedded in a large anodic area, consequently, accelerating corrosion propagation, either intergranular or intragranular.[5,12,22,34]

After initial dissolution, the sub-grains are exposed to a corrosive environment leading to corrosion propagation under a covered surface, until the surface is detached from the substrate due to a large volume difference between corrosion products and the matrix.

The influence of the T1 phase (Al_2CuLi) on the severe localized corrosion of the Al-Cu-Li alloys is easily observed for the exposed surfaces to EXCO solution by comparing with that of the exposed Al-Cu-Mg alloy, Figure 5. In the same sense, the weight-loss differences are due to the T1 phase in the Al-Cu-Li alloys and SVET maps.

The comparison between the tested Al-Cu-Li and Al-Cu-Mg alloys must consider that the microstructures of the two alloys are completely different. The T1 phase is found only in the Li-containing alloy and it precipitates preferentially within some of the grains, according to their crystallographic orientation, leaving the neighborhood depleted in copper. This increases susceptibility to intergranular and intragranular corrosion. The intragranular attack might lead to reduced corrosion penetration. Li seems to have an important role in the mechanism of corrosion penetration into the alloy.

The lower resistance to severe localized corrosion presented by the AA2050-T84 when compared to AA2198-T851 (both Al-Cu-Li alloys) could be related to a difference in the intermetallic particle distribution in these alloys with the AA2050 presenting a higher number of particles per area and tendency to agglomeration, Figure 8. As stated earlier, the nucleation process is associated with these particles that act as preferential sites of corrosion propagation.

Table 2 summarizes the main findings of each immersion test condition and the severity of the corrosive attack.

5 | CONCLUSIONS

The results of this study pointed out a correlation between microstructure and the development of severe localized corrosion in Al-Cu-Li alloys. The micrometric constituent particles played a major role in the initiation of corrosion, and their distribution has a correlation with the severe localized corrosion intensity.

After corrosion initiation by microgalvanic effects due to Cu-rich micrometric particles at the surface, corrosion propagation is dependent on the microstructure of the alloy. The initial corrosion mechanism is due to microgalvanic coupling at the surface between the matrix and the Cu-Fe enriched particles and the matrix. This leads to preferential dissolution of Li and Al relative to Cu, but later, reversal polarity, due to Cu enrichment in the particles. Subsequently, trenching occurs due to the Cu-enriched particles acting as cathodic sites relative to the matrix that is preferentially attacked.

Corrosion propagation in Al-Cu-Li alloys is related to the nanometric T1 phase (Al_2CuLi) particles, which might lead to either intragranular or intergranular attacks, depending on the preferential localization of the T1 phase.

ACKNOWLEDGEMENTS

The authors are thankful to CNPq for the financial support for this project (CNPq Proc 406871/2021-3) and for the grant awarded to Rafael E. Klumpp (CNPq Proc 200257/2022-6) and to the SPW-Economie Emploi Recherche – Wallonie in the framework of the program OptiSurFam – Win2Wal (2310020). Additionally, appreciation is extended to the Fundação de Amparo à Pesquisa do Estado de São Paulo (FAPESP), [Process 2019/18388-1] Grant of João V.S. Araujo, and to the Fédération Wallonie-Bruxelles (Actions de Recherche Concertées ARC SEALCERA – Grant of Sajjad Akbarzadeh).

DATA AVAILABILITY STATEMENT

The data that support the findings of this study are available from the corresponding author upon reasonable request.

REFERENCES

1. Dursun T, Soutis C. Recent developments in advanced aircraft aluminium alloys. *Mater des*. 2014;56:862-871. doi:10.1016/j.matdes.2013.12.002
2. Rambabu P., Eswara Prasad N., Kutumbarao V. V. and Wanhill R. J. H., 2017, pp. 29–52.
3. Araujo JV d S, da Silva RMP, de Viveiros BVG, Klumpp RE, Costa I. Estudo do comportamento eletroquímico de uma liga Al-Cu-Li. *Matéria (Rio Janeiro)*. 2024;29:e20230328. doi:10.1590/1517-7076-rmat-2023-0328
4. Wanhill R. J. H. and Bray G. H., in *Aluminum - Lithium Alloys: Processing, Properties, And Applications*, eds. N. E. Prasad, A. Gokhale and R. J. H. Wanhill, Elsevier Inc. 2014, pp. 27–58, doi:10.1016/B978-0-12-401698-9.00002-1.
5. Milagre M. X., Araujo J. V. de S., Pereira M., Donatus U., Machado C. S. C. and Costa I., in *Proceedings of the European Corrosion Congress*, 2018.
6. Donatus U. Corrosion behaviour of friction stir welded aluminium alloys: unpredictability and protection. *Res Dev Mater Sci*. 2017;2:1-3.
7. Sousa Araujo JV, Milagre MX, Ferreira RO, et al. Exfoliation and intergranular corrosion resistance of the 2198 Al–cu–Li alloy with different thermomechanical treatments. *Mater Corros*. 2020;71(12):1957-1970. doi:10.1002/maco.202011839
8. Birbilis N, Buchheit RG. Electrochemical characteristics of intermetallic phases in aluminum alloys. *J Electrochem Soc*. 2005;152(4):B140. doi:10.1149/1.1869984
9. Donatus U, Bodunrin MO, Olayinka A, et al. *Advanced Aluminium Composites and Alloys*; 2021:159.
10. Correia AN, Braga DFO, Moreira PMGP, Infante V. Review on dissimilar structures joints failure. *Eng Fail Anal*. 2021;129:1-14, 105652. doi:10.1016/j.engfailanal.2021.105652
11. Owolabi GM, Thom M, Ajide O, et al. Fatigue responses of three AA 2000 series aluminum alloys. *J Mater Sci Chem Eng*. 2019;07(03):32-48. doi:10.4236/msce.2019.73003
12. Buchheit RG, Moran JP, Stoner GE. Localized corrosion behavior of alloy 2090—the role of microstructural heterogeneity, corrosion. 1990;46(8):610-617. doi:10.5006/1.3585156
13. Buchheit RG, Moran JP, Stoner GE. Electrochemical behavior of the T 1 (Al 2 CuLi) intermetallic compound and its role in localized corrosion. *Corros Sci*. 1994;50(2):120-130. doi:10.5006/1.3293500
14. Ma Y, Zhou X, Huang W, et al. Crystallographic defects induced localised corrosion in AA2099-T8 aluminium alloy. *Corros Eng Sci Technol*. 2015;50(6):420-424. doi:10.1179/1743278214Y.0000000237
15. Zhang X, Zhou X, Hashimoto T, et al. The influence of grain structure on the corrosion behaviour of 2A97-T3 Al-Cu-Li alloy. *Corros Sci*. 2017;116:14-21. doi:10.1016/j.corsci.2016.12.005
16. Huang J, Li J, Liu D, et al. Correlation of intergranular corrosion behaviour with microstructure in Al-Cu-Li alloy. *Corros Sci*. 2018;139:215-226. doi:10.1016/j.corsci.2018.05.011
17. Milagre MX, Donatus U, Mogili NV, et al. Galvanic and asymmetry effects on the local electrochemical behavior of the 2098-T351 alloy welded by friction stir welding. *J Mater Sci Technol*. 2020;45:162-175. doi:10.1016/j.jmst.2019.11.016
18. Donatus U, Ferreira RO, Mogili NVV, de Viveiros BVG, Milagre MX, Costa I. Corrosion and anodizing behaviour of friction stir weldment of AA2198-T851 Al-Cu-Li alloy. *Mater Chem Phys*. 2018;219:493-511. doi:10.1016/j.matchemphys.2018.08.053
19. Donatus U, de Sousa Araujo JV, de Souza Carvalho Machado C, Vardhan Mogili NV, Antunes RA, Costa I. The effect of manufacturing process induced near-surface deformed layer on the corrosion behaviour of AA2198-T851 Al–Cu–Li alloy. *Corros Eng Sci Technol*. 2018;2782(3):1-11. doi:10.1080/1478422X.2018.1558932
20. Viveiros BVGD, Donatus U, de Alencar MC, Berbel LO, Costa I. Comparing the corrosion behaviour of AA2050 and AA7050 aluminium alloys by scanning vibrating electrode and scanning ion-selective electrode techniques. *Corros Eng Sci Technol*. 2022;57(1):85-96. doi:10.1080/1478422X.2021.1992132
21. Zhang S, Zeng W, Yang W, Shi C, Wang H. Ageing response of a Al-Cu-Li 2198 alloy. *Mater des*. 2014;63:368-374.
22. Buchheit RG, Grant RP, Hiava PF, Mckenzie B, Zender G. Local dissolution phenomena associated with S phase (Al2CuMg) particles in aluminum alloy 2024-T3. *J Electrochem Soc*. 1997;144(8):2621-2628. doi:10.1149/1.1837874
23. Donatus U, de Viveiros BVG, de Alencar MC, et al. Correlation between corrosion resistance, anodic hydrogen evolution and microhardness in friction stir weldment of AA2198 alloy. *Mater Charact*. 2018;144:99-112. doi:10.1016/j.matchar.2018.07.004
24. de Souza Carvalho Machado C, da Silva RMP, de Sousa Araujo JV, et al. Influence of chloride ions concentration on the development of severe localised corrosion and its effects on the electrochemical response of the 2198-T8 alloy. *Corros Eng Sci Technol*. 2021;56(4):341-350. doi:10.1080/1478422X.2020.1862390
25. da Silva RMP, Milagre MX, de Oliveira LA, Donatus U, Antunes RA, Costa I. The local electrochemical behavior of the AA2098-T351 and surface preparation effects investigated by scanning electrochemical microscopy. *Surf Interface Anal*. 2019;51(10):982-992. doi:10.1002/sia.6682
26. Alexopoulos ND, Proiou A, Dietzel W, et al. Mechanical properties degradation of (Al-Cu-Li) 2198 alloy due to corrosion exposure. *Procedia Struct Integr*. 2016;2:597-603. doi:10.1016/j.prostr.2016.06.077
27. Queiroz FM, Magnani M, Costa I, de Melo HG. Investigation of the corrosion behaviour of AA 2024-T3 in low concentrated chloride media. *Corros Sci*. 2008;50(9):2646-2657. doi:10.1016/j.corsci.2008.06.041
28. de Abreu CP, Costa I, de Melo HG, Pébère N, Tribollet B, Vivier V. Multiscale electrochemical study of welded Al alloys joined by friction stir welding. *J Electrochem Soc*. 2017;164(13):C735-C746. doi:10.1149/2.0391713jes
29. Bugarin AFS, Queiroz FM, Terada M, De Melo HG, Costa I. Localized corrosion resistance of dissimilar aluminum alloys joined by friction stir welding (FSW). *Key Eng Mater*. 2016;710:41-46. doi:10.4028/www.scientific.net/KEM.710.41
30. Bousquet E, Poulon-Quintin A, Puiggali M, Devos O, Touzet M. Relationship between microstructure, microhardness and corrosion

sensitivity of an AA 2024-T3 friction stir welded joint. *Corros Sci*. 2011;53(9):3026-3034. doi:10.1016/j.corsci.2011.05.049

31. Palomino LEM. Caracterização microestrutural e eletroquímica de revestimentos ambientalmente amigaveis aplicados sobre a liga de AL2024-T3 - [Tese]. 2007;265.
32. Alam MP, Sinha AN. Fabrication of third generation Al–Li alloy by friction stir welding: a review. *Sadhana - Acad Proc Eng Sci*. 2019; 44(6):1-13, 153. doi:10.1007/s12046-019-1139-4
33. Machado C d SC, Donatus U, Giorjão RAR, et al. *Proceedings of the European Corrosion Congress*; 2018:26.
34. Milagre MX, Mogili NV, Donatus U, et al. On the microstructure characterization of the AA2098-T351 alloy welded by FSW. *Mater Charact*. 2018;140:233-246. doi:10.1016/j.matchar.2018.04.015
35. Lu D, Li J, Ning H, et al. Effects of microstructure on tensile properties of AA2050-T84 Al – Li alloy. *Trans Nonferrous Met Soc Chin*. 2021;31(5):1189-1204. doi:10.1016/S1003-6326(21)65571-1
36. Prasad KS, Prasad NE, Gokhale AA. *Aluminum - Lithium Alloys*. Elsevier Inc.; 2014:99-137. doi:10.1016/B978-0-12-401698-9.00004-5
37. Jagadeesh C. Effect of multi-directional forging on the evolution of microstructural and mechanical properties of lightweight Al-Cu-Li alloy AA2050. *J Mater Eng Perform*. 2023;1–15(24):11118-11132. doi:10.1007/s11665-023-07922-5
38. Proton V, Alexis J, Andrieu E, et al. The influence of artificial ageing on the corrosion behaviour of a 2050 aluminium-copper-lithium alloy. *Corros Sci*. 2014;80:494-502. doi:10.1016/j.corsci.2013.11.060
39. Donatus U, Terada M, Ospina CR, Queiroz FM, Bugarin AFS, Costa I. On the AA2198-T851 alloy microstructure and its correlation with localized corrosion behaviour. *Corros Sci*. 2018;131:300-309. doi:10.1016/j.corsci.2017.12.001
40. Donatus U, Klumpp RE, Vardan Mogili NV, Antunes RA, Milagre MX, Costa I. The effect of surface pretreatment on the corrosion behaviour of silanated AA2198-T851 Al-Cu-Li alloy. *Surf Interface Anal*. 2019;51(2):275-289. doi:10.1002/sia.6584
41. Donatus U, da Silva RMP, Araujo JV d S, et al. Macro and microgalvanic interactions in friction stir weldment of AA2198-T851 alloy. *J Mater Res Technol*. 2019;8(6):6209-6222. doi:10.1016/j.jmrt.2019.10.015
42. Steuwer A, Dumont M, Altenkirch J, et al. A combined approach to microstructure mapping of an Al-Li AA2199 friction stir weld. *Acta Mater*. 2011;59(8):3002-3011. doi:10.1016/j.actamat.2011.01.040
43. Proton V, Alexis J, Andrieu E, Delfosse J, Lafont M-C, Blanc C. Characterisation and understanding of the corrosion behaviour of the nugget in a 2050 aluminium alloy friction stir welding joint. *Corros Sci*. 2013;73:130-142. doi:10.1016/j.corsci.2013.04.001
44. Machado CSC, Klumpp RE, Ayusso VH, et al. Effect of surface treatments on the localized corrosion resistance of the AA2198-T8 aluminum lithium alloy welded by FSW process. *Surf Interface Anal*. 2019; 51(12):1231-1239. doi:10.1002/sia.6622
45. Klumpp RE, Donatus U, Araujo JVS, Redígolo MM, Machado C d SC, Costa I. The effect of acid pickling on the corrosion behavior of a cerium conversion-coated AA2198-T851 Al-Cu-Li alloy. *J Mater Eng Perform*. 2020;29(1):167-174. doi:10.1007/s11665-019-04551-9

SUPPORTING INFORMATION

Additional supporting information can be found online in the Supporting Information section at the end of this article.

How to cite this article: Klumpp RE, Akbarzadeh S, JV de Sousa Araujo, et al. Correlating corrosion modes with the microstructure of the 2XXX series alloys: A comparative approach. *Surf Interface Anal*. 2024;1-11. doi:10.1002/sia.7321